Materials Science & Engineering A 782 (2020) 139255

Contents lists available at ScienceDirect

Materials Science & Engineering A

journal homepage: http://www.elsevier.com/locate/msea

On the influence of crystallography on creep of circular notched single crystal superalloy specimens

L. Cao [a,*], P. Thome [a], L. Agudo Jácome [b], C. Somsen [a], G. Cailletaud [c], G. Eggeler [a]

[a] Institut für Werkstoffe, Ruhr-Universität Bochum, Universitätsstr. 150, 44801, Bochum, Germany
[b] Bundesanstalt für Materialforschung und -prüfung (BAM), Abteilung für Werkstofftechnik, Unter den Eichen 87, 12205, Berlin, Germany
[c] Mines Paristech, PSL Research University, Centre des Materiaux, CNRS UMR 7633, 63-65 Rue Henri Auguste Desbrueres, 91003, Evry Cedex, France

ARTICLE INFO

Keywords:
Single crystal Ni-Base superalloys
Double notched creep specimen
Stress distribution
Lattice rotation
Cracks
Fracture

ABSTRACT

The present work contributes to a better understanding of the effect of stress multiaxiality on the creep behavior of single crystal Ni-base superalloys. For this purpose we studied the creep deformation and rupture behavior of double notched miniature creep tensile specimens loaded in three crystallographic directions [100], [110] and [111] (creep conditions: 950 °C and 400 MPa net section stress). Crystal plasticity finite element method (CPFEM) was used to analyze the creep stress and strain distributions during creep. Double notched specimens have the advantage that when one notch fails, the other is still intact and allows to study a material state which is close to rupture. No notch root cracking was observed, while microstructural damage (pores and micro cracks) were frequently observed in the center of the notch root region. This is in agreement with the FEM results (high axial stress and high hydrostatic stress in the center of the notched specimen). Twinning was observed in the notch regions of [110] and [111] specimens, and <112> {111} twins were detected and analyzed using orientation imaging scanning electron microscopy. The present work shows that high lattice rotations can be detected in SXs after creep fracture, but they are associated with the high strains accumulated in the final rupture event.

1. Introduction

Ni-base single crystal superalloys (SXs) are used to make blades for gas turbines operating in aero engines and in fossil fired power plants [1–7]. In service, gas turbine blades must withstand mechanical loads at temperatures close to the melting point of superalloys, where creep, the time dependent plastic deformation of metals [8–14], determines their service life. Due to the complex geometry and thermal gradients, stress states are not homogeneous. Therefore, mechanical engineers and material scientists are interested in the creep behavior of materials under multiaxial stress states [15–22]. In the present work we focus on circular notches, which produce triaxial stress states [23–27]. It is known that stress redistribution occurs in circular notched specimens during creep [28–35]. While there are high axial stresses in the notch root directly after loading, creep stress redistribution eventually results in a relatively more homogeneous triaxial stress state.

We have recently used circular notched <001> miniature tensile creep specimens to investigate the differences between the creep behavior of uniaxial and circular notched creep specimens at same creep temperature and net section stress [35]. We also investigated how the kinetics of rafting is influenced by the redistribution of stresses in circular notched specimens [36] tested at 950 °C and a net section of 300 MPa. These creep conditions were proven to be experimentally convenient for studying the evolution of microstructure by investigating specimens from interrupted creep experiments.

The present study was motivated by the work of Boubidi [37] with SC16 notched specimens, and of Basoalto et al. [38,39] and Ardakani et al. [40,41], who used circular double notched specimens for creep testing of superalloy single crystals. They conducted creep tests on uniaxial and double notched specimens loaded along <001>, <011> and <111> directions at 850 °C and stress levels between 600 and 850 MPa. They reported that the creep life of notched specimens was one order of magnitude longer than that of uniaxial specimens. Another conclusion was that lattice rotations up to 20° can be observed in ruptured circular notched specimens. Lattice rotations in single crystal superalloys have already been studied for uniaxial creep specimens [42–45]. Ardakani et al. [42] reported that almost no lattice rotation occurred in specimens uniaxially stressed in the [001] and [111]

* Corresponding author.
E-mail address: Lijie.Cao@rub.de (L. Cao).

https://doi.org/10.1016/j.msea.2020.139255
Received 10 January 2020; Received in revised form 29 February 2020; Accepted 15 March 2020
Available online 19 March 2020

Table 1
Average chemical composition of single crystal superalloy ERBO/1 in wt.%.

Al	Co	Cr	Hf	Mo	Re	Ta	Ti	W	Ni
5.8	9.3	6.2	0.1	0.6	2.9	6.9	1.0	6.3	Bal.

directions, while large lattice rotations were observed in a specimen loaded along [011] direction. McLean et al. [45] predicted that specimens of simple symmetric orientations exhibit little orientation change after creep exposure, while complex orientations or multiaxial stresses can result in large lattice rotations.

Our previous work [35,36] showed that up to 306 h creep time, circular notched specimens only accumulated limited amount of creep strain at 950 °C and a net section stress of 300 MPa. This sheds doubt on the high degree of lattice rotations reported by Basoalto et al. [38,39] and Ardakani et al. [40,41]. The present work has three main objectives. First, to find out whether the high lattice rotations are associated with creep deformation, or whether they represent the geometric changes which occur during the final rupture event. This will be investigated using a novel circular double notched miniature tensile creep specimen. Second, the influence of crystallography on creep rupture will be investigated by testing double notched miniature specimens loaded

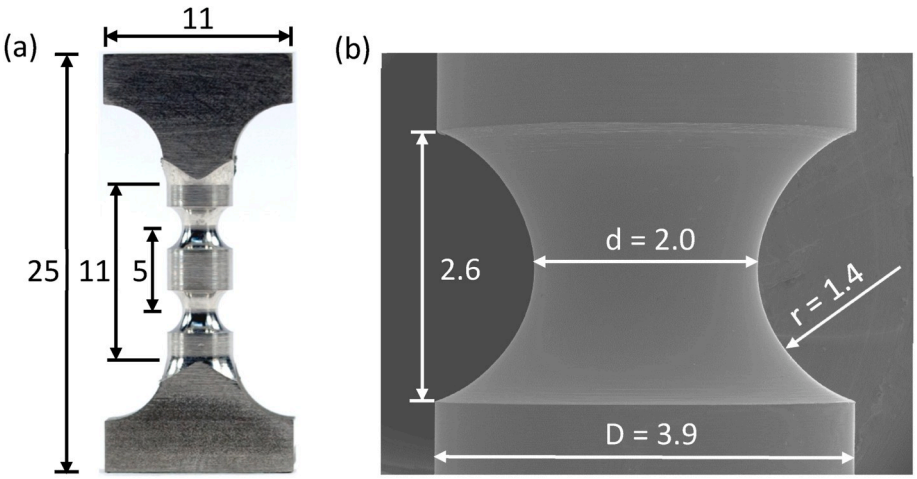

Fig. 1. Double notch specimen investigated in the present work. (a) Photograph of specimen after machining. (b) SEM image of one of the two circular notches at a higher magnification. All dimensions given in mm.

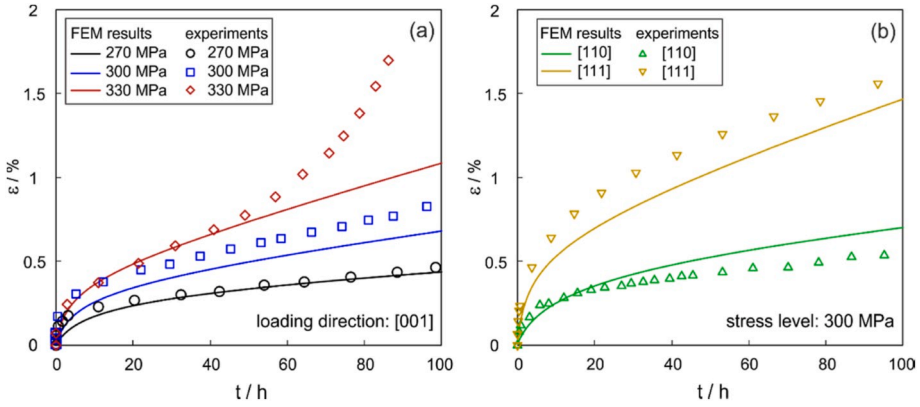

Fig. 2. Examples for reasonable agreement between experimental and FEM creep curves prior to the onset of tertiary creep at 950 °C. Creep data are shown as strain ε vs. time t. (a) Stress dependence of [001] tensile creep (stresses: 270, 300 and 330 MPa as indicated). (b) Influence of crystallography on creep: [110] and [111] tensile creep data obtained for a stress of 300 MPa ([001] data see Fig. 2a). The empty symbols represent the experimental data [51], the solid lines show the simulation results.

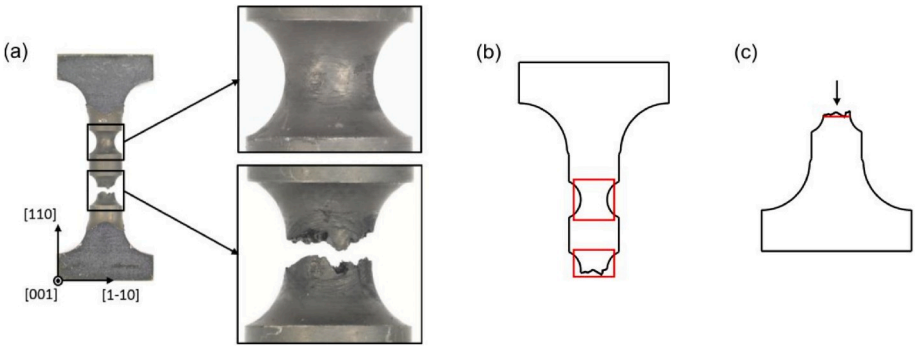

Fig. 3. (a) Ruptured [110] double notched tensile miniature creep specimen. (b) Schematic showing the longitudinal cross section of the longer part. (c) Schematic indicating the transverse cross section of the shorter part. The areas investigated with EBSD are indicated with red lines.

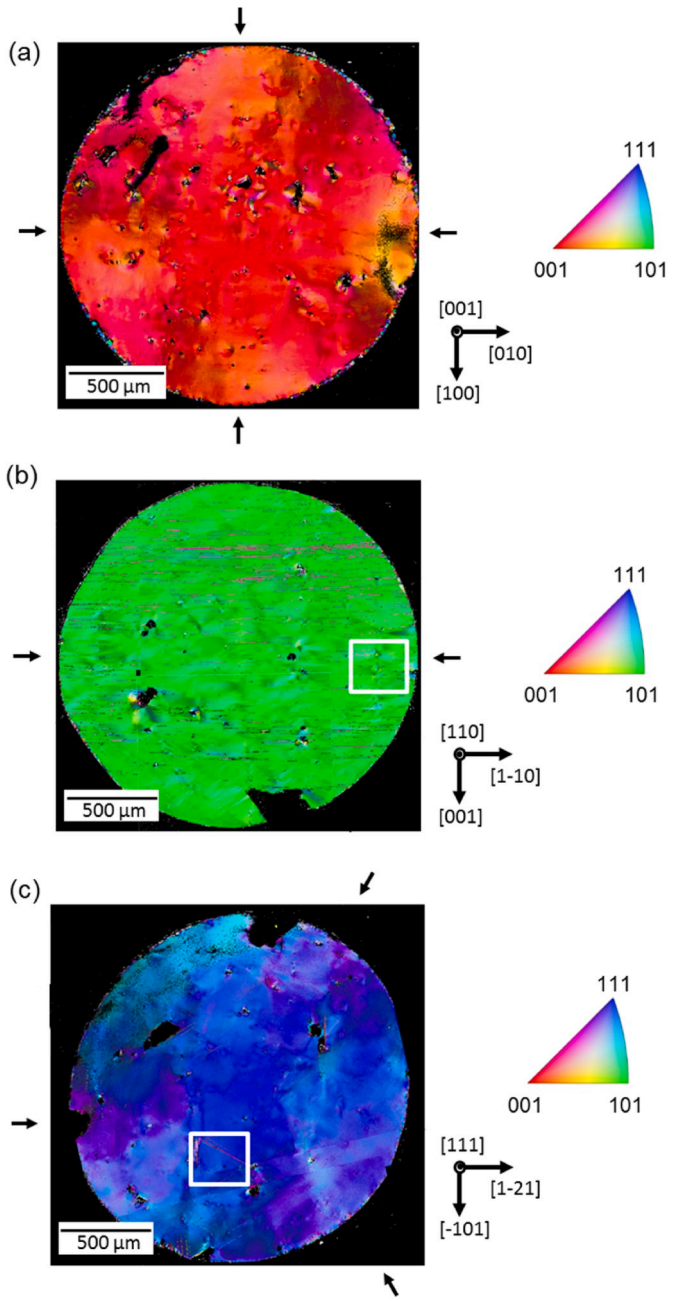

Fig. 4. Color coded EBSD results obtained from the transverse cross sections shown in Fig. 3c for the three tensile loading directions: (a) [001]. (b) [110]. (c) [111].

along [001], [110] and [111] crystallographic directions. Finally, attention will be paid to whether or not notch root cracking occurs in the circular notched specimens. When creep rupture occurs in one of the two notches, the other notch is still intact. There is a natural scatter in creep rupture times, which is related to the stochastic nature of creep damage accumulation, which was discussed in the literature [46,47]. However, this second notch is close to rupture and this allows to analyze microstructures shortly before rupture, in the absence of the high local plastic strains associated with the final rupture.

2. Material and experiments

2.1. Material

The material investigated in the present work is the Ni-base single crystal superalloy ERBO/1 (CMSX4-type). Its average chemical composition is given in Table 1. The initial state microstructure consists of cuboidal γ'-particles (typical volume fraction: 75 %, crystal structure: $L1_2$ phase) and thin γ-channels (typical volume fraction: 25 %, crystal structure: FCC). The details of heat treatment and the initial state microstructure have been documented elsewhere [48].

2.2. Creep testing with double notched miniature tensile specimens

The double notched miniature tensile creep specimens studied in the present work were developed based on our previous work [35,49] and following the recommendations from the code of practice for notched bar testing [50]. Three key factors were considered. First, the distance between the two notches should be large enough, so that the stress fields of both notches do not interfere with each other during creep. Second, the size of the specimens should be as small as possible which allows to take out specimens in different crystallographic directions from a standard sized laboratory slab or bar. Moreover, the specimen dimensions should be large enough to allow reproducible specimen manufacturing.

To manufacture the double notched specimens, an iterative procedure is used [51]: First the material is aligned precisely using a Laue camera. Oriented uniaxial miniature specimens are then machined using electro discharge machining (EDM). Afterwards, notches are machined into these specimens in a computer numerically controlled (CNC) high precision lathe. We follow the procedure described in our previous work [35], except that two notches are machined instead of only one. Fig. 1a shows a photograph of the miniature double notched specimen after machining, and Fig. 1b shows a scanning electron microscope (SEM) image of the notch region at a higher magnification. The double notched specimen has a total length of 25 mm and an effective gauge length of 11 mm, with a cylindrical cross section (shaft diameter D = 3.9 mm), and two circular notches (notch root diameter d = 2 mm and notch radius r = 1.4 mm). The regions of the circular notches are polished using a 1 µm diamond suspension in the last polishing step. In the present work we perform tensile creep tests until rupture at 950 °C and a net section stress of 400 MPa. Details of creep testing (heating rate, pre-load, time a temperature to establish thermal equilibrium, application of load, position of thermocouples, etc.) are reported elsewhere [51].

2.3. Finite element creep stress and strain calculations

To study the stress and strain distributions in the double notched specimens during creep, finite element (FE) calculations are performed using the FE code Z-set. An anisotropic visco-plastic crystallographic phenomenological model from Meric and Cailletaud [52,53] is used, which accounts for yield, primary and secondary creep. FEM modelling was used to help rationalize the crystallographic shape changes of the specimens when loaded in different crystallographic directions. The total strain $\underset{\sim}{\varepsilon}$ is partitioned into elastic $\underset{\sim}{\varepsilon}^e$ and plastic strain $\underset{\sim}{\varepsilon}^p$:

$$\underset{\sim}{\varepsilon} = \underset{\sim}{\varepsilon}^e + \underset{\sim}{\varepsilon}^p \tag{1}$$

The elastic strain $\underset{\sim}{\varepsilon}^e$ follows Hooke's law:

$$\underset{\sim}{\varepsilon}^e = \underset{\approx}{C}^{-1} : \underset{\sim}{\sigma} \tag{2}$$

where $\underset{\sim}{\sigma}$ is the stress tensor, and $\underset{\approx}{C}$ is the fourth-order tensor of the elastic modulus.

The evolution of the plastic slip rate $\dot{\gamma}^s$ is controlled by a classical

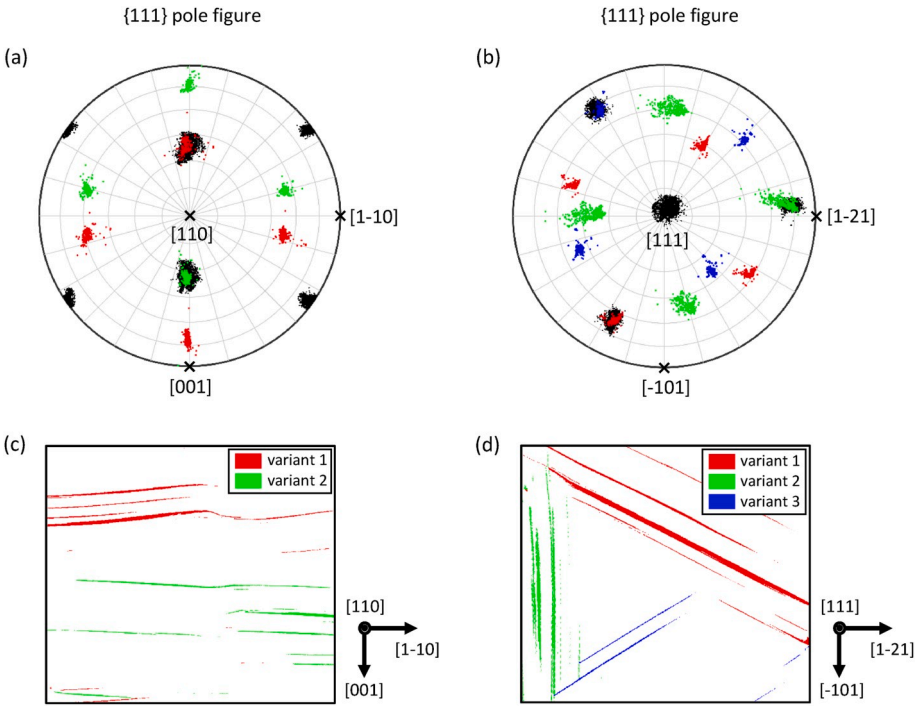

Fig. 5. Twin analysis in the transverse cross sections of the failed notches. (a) and (b) {111} pole figures indicating the matrix and different twin variants. (c) and (d) Twin bands showing different variants indicated by different colors. (a) and (c) [110] tensile loading. (b) and (d) [111] tensile loading.

power law expression:

$$\dot{\gamma}^s = \langle \frac{|\tau^s - \chi^s| - r^s}{K} \rangle^n \mathrm{sgn}(\tau^s - \chi^s) \tag{3}$$

where χ^s is the kinematic hardening, r^s is the isotropic hardening, and τ^s is the resolved shear stress acting in the slip system s, which is the scalar product of the stress tensor $\underset{\sim}{\sigma}$ by the orientation tensor $\underset{\sim}{m}^s$:

$$\tau^s = \underset{\sim}{\sigma} : \underset{\sim}{m}^s \tag{4}$$

$\underset{\sim}{m}^s$ is calculated as

$$\underset{\sim}{m}^s = \frac{1}{2}(\underline{n}^s \otimes \underline{l}^s + \underline{l}^s \otimes \underline{n}^s) \tag{5}$$

where $\underline{n}^s$ represents the normal to the slip plane, and $\underline{l}^s$ the slip direction for the slip system s. The macroscopic plastic strain rate $\dot{\varepsilon}^p$ results as the sum of the plastic slip contributions from all N slip system s.

$$\dot{\varepsilon}^p = \sum_{s=1}^{N} \dot{\gamma}^s \underset{\sim}{m}^s \tag{6}$$

In the present work plastic deformation is assumed to take place by dislocation glide. Two families of slip systems are taken into consideration, 12 octahedral slip systems {111} <1–10> and 6 cubic slip systems {001} <110>. Linear isotropic and kinematic hardening are considered, and slip system interaction is neglected.

The parameters of the model used in the present work have been calibrated for uniaxial tensile creep data of the single crystal superalloy ERBO/1 in the temperature range of 950 °C. A large number of uniaxial creep tests for ERBO/1 have been carried out and reported in the work of Wollgramm et al. [51]. Fig. 2 shows the comparison of the experimental and numerical tensile creep curves. The empty symbols represent the experimental data and the solid lines show the simulation results. It can be seen that the uniaxial experimental and calculated strain values are in reasonable agreement, as long as the experimental data are not strongly affected by tertiary creep processes, as is the case for the 330 MPa data in Fig. 2a. In the present work we will use our FEM procedure to rationalize crystallographic shape changes in circular notched specimens. Due to the symmetry of the double notched specimen, only one notch is included in the FE calculation. 20-nodes 3D continuum elements (C3D20) are used in the finite element mesh (for details see manual of Z-set [54]).

2.4. Scanning electron microscopy (SEM) and electron back-scattered diffraction (EBSD)

When a double notched specimen fails, rupture occurs in only one of the two notches, while the other one is close to rupture. Fig. 3a shows the ruptured [110] double notched creep specimen. The specimen failed in the region of the lower notch while the upper notch is still intact. The rupture surface in the failed part of the specimen is not even, but its direction scatters around the minimum diameter cross section. Local shear events and shear steps can be clearly observed, which are just about to be recognizable in the intact notch region. The specimens loaded along the [001] and [111] directions are not shown here, but their ragged rupture surfaces also follow the minimum diameter cross sections.

In the present work, a scanning electron microscope (SEM) of type Leo Gemini 1530 from Carl Zeiss AG is used to clarify the microstructural and crystallographic features, which govern fracture in the three loading directions [001], [110] and [111]. In a first step, the rupture surface features are documented. Then two types of cross sections are prepared, as schematically illustrated in Fig. 3b and c. One cross section was taken parallel to the loading direction from the center of the test bar, such that both the failed and the intact notch regions are intersected, Fig. 3b. The normal directions of these cross sections were [100] for the [001] loading direction, and [001]/[-101] for the [110]/[111] loading directions, respectively. Another cross section was prepared perpendicular to the loading direction as close as possible to the rupture surface from the failed part of the specimen, Fig. 3c.

The areas indicated by the red lines (2D projection of close to notch root circle) in Fig. 3c and the two red squares in Fig. 3b were prepared

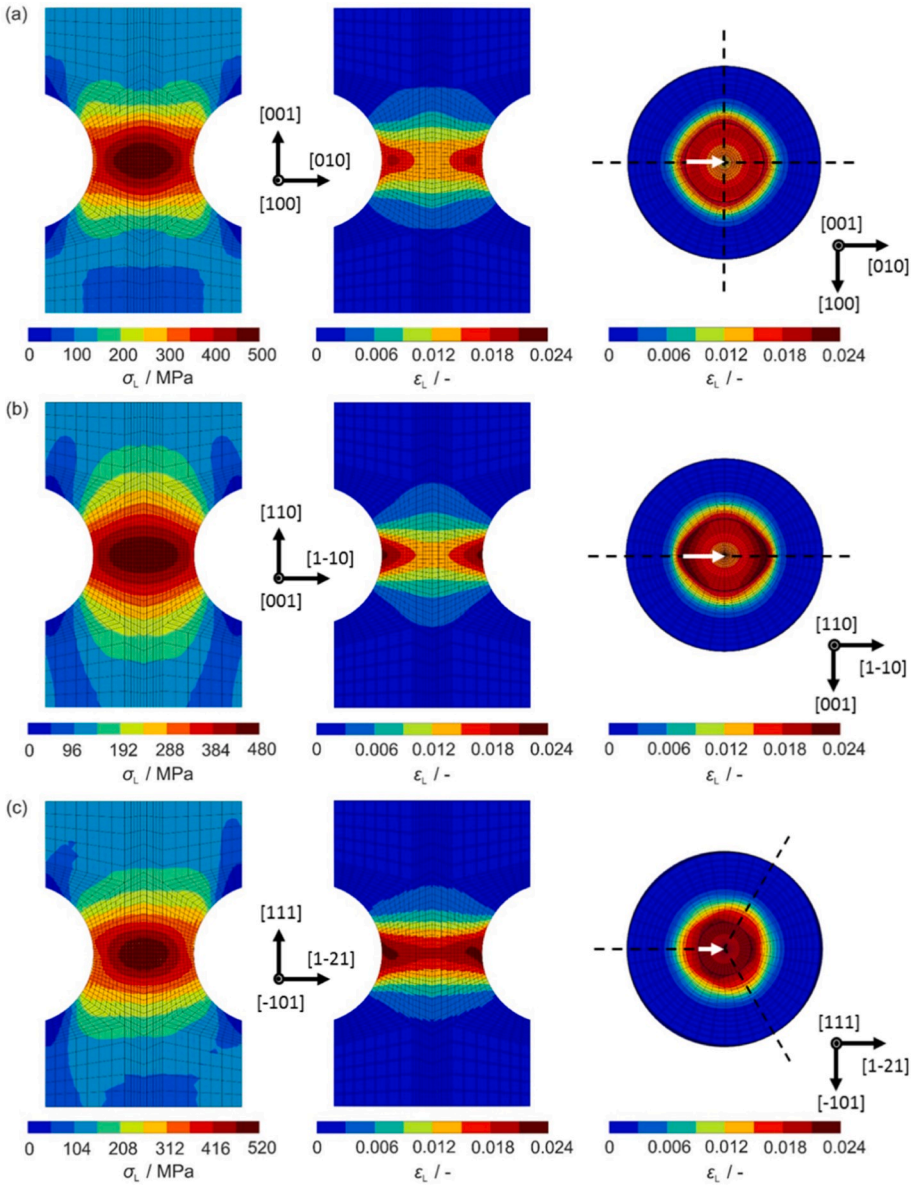

Fig. 6. FEM results showing the stress and strain distributions (400 MPa net section stress and a creep period of 80 h). Left column: Axial stresses σ_L in central longitudinal cross sections. Middle column: Axial strains ε_L in central longitudinal cross sections. The crystallographic orientations given for each loading direction apply for both left and right images. Right column: Axial strains presented in transverse cross sections (crystallographic directions given). In order to outline the effects clearly, deformations were magnified by factors of 30 (for [001] and [110] loading direction) and 50 (for [111] loading direction).

for high resolution orientation imaging. For this purpose, the cross sections were polished with diamond suspension until 1 μm, and then vibropolished for 5 h (Vibromet 2, Buehler, Esslingen, Germany) in colloidal silica suspension MasterMet 2 with a particle size of 0.02 μm. Then electron back-scattered diffraction (EBSD) scans were performed using a SEM of type QUANTA 650 from FEI, equipped with a field emission gun. During the EBSD measurements, the specimens were tilted by 70° and an acceleration voltage of 30 kV was used at a working distance about 17 mm. The EBSD measurements were performed using a Hikari XP camera from EDAX Inc. The EBSD data are analyzed with the free MATLAB [55] toolbox MTEX [56,57]. Examples of EBSD results obtained in the present work are shown in Fig. 4, for the type of cross section shown in Fig. 3c. The plane normal of the three idealized cross section planes represent the creep loading directions. The color coding in Fig. 4 reveals a 4-fold symmetry after [001] and a 3-fold symmetry after [111] tensile creep testing. We will come back to this point later. Wrongly indexed data points and points from the embedding mass were identified using a manually adjusted threshold for the confidence index (CI index) and are presented as black regions in Fig. 4. The data sets were additionally rotated around the cross section normal (ND axis) to align the principal crystal axes with the reference coordinate systems, see Fig. 4.

Moreover, an effort was made to analyze local deformation events. To quantify the local deviations from the average reference orientation, the data sets were analyzed in four steps. First, a grain reconstruction procedure was applied with an angular threshold of 5° to separate matrix orientations from orientations associated with twins. In a second step, the resulting data were presented in pole figures, Fig. 5a and b. The pole figures in Fig. 5a and b show results which were obtained for [110] and [111] loading. The six black point groups in Fig. 5a correspond to the four {111} planes of the matrix (there are only four but two appear on both sides of the projection). The four green and red data point groups represent {111} planes associated with the two twin variants. The directions where they coincide with the black data points of the matrix represents the twin planes. Two and three twin systems can thus be clearly identified during [110] and [111] loading, Fig. 5a and b. The colors introduced in Fig. 5a and b are used in the microstructural maps shown in Fig. 5c and d.

In the third step, we calculated the average orientations of all matrix data points. Then, in the fourth step, the misorientations of all valid points were calculated relative to the determined average matrix orientation. The resulting data can then be plotted as color coded maps,

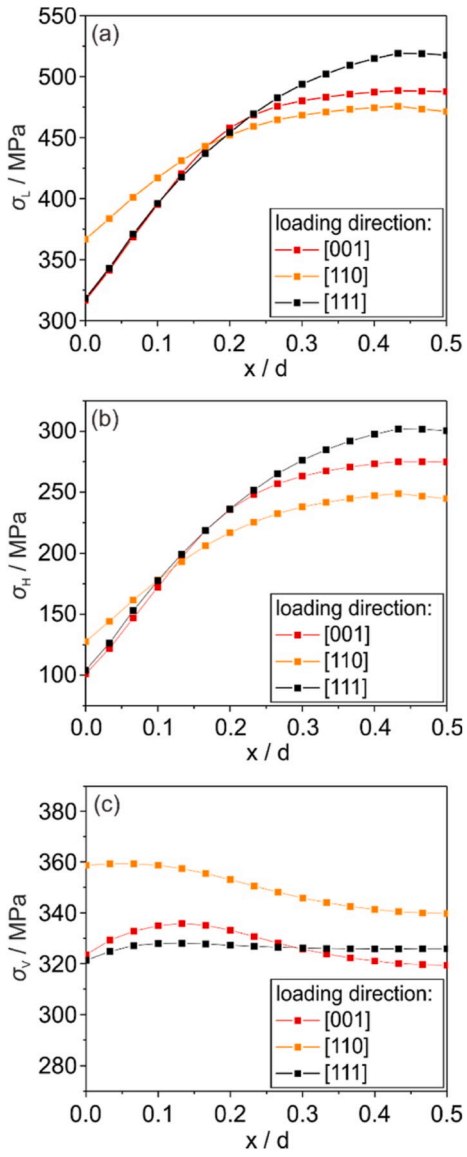

Fig. 7. Comparison of the axial stress, the hydrostatic stress and the von Mises stress at different positions of the notch root cross section. The results were obtained for directions along the white arrows shown in Fig. 5, starting in the notch root (distance x normalized by cross section diameter d equals 0: x/d = 0) and ending in the center of the specimen (x/d = 0.5). (a) Axial stress σ_L. (b) Hydrostatic stress σ_H. (c) Von Mises stress σ_V.

Fig. 5c and d. Moreover, we identified the presence of twins for some selected data sets. For this purpose, we make use of the grain segmentation performed earlier to isolate the average orientations of the different twin variants by using the orientation density function (ODF) provided by the MTEX software. We isolated the orientation of the twin variants and plotted each variant orientation and represent the results by using a unique color in a {111} pole figure, Fig. 5a and b. Finally we account for the frequency of grain boundary misorientation angles in a histogram and misorientation axes in an inverse pole figure, Fig. 13.

3. Results

Stress and strain distributions: Fig. 6 shows stress and strain distributions in the notch regions for the three loading directions which were calculated using the FEM procedure described above for a net section stress of 400 MPa and a creep exposure time of 80 h. We present three color coded images for each loading direction. Fig. 6a shows the FEM creep stress and strain analysis results for the [001] loading direction. The left image shows the distribution of the axial stress σ_L in the central longitudinal cross section as described in Fig. 3b. The image in the middle presents the corresponding distribution of the axial strain ε_L. The crystallographic orientations which apply to both images are indicated between the two figures. The figure on the right shows the axial strain plotted in the transverse cross section of the type shown in Fig. 3c (crystallographic axis indicated below the figure, for better visibility the deformation effect is magnified). This figure allows to appreciate the 4-fold symmetry associated with the [001] loading direction. The white arrow which points into [010] direction will be referred to later. Fig. 6b and c show the results for [110] and [111] loading directions, the results in the transverse cross sections (magnified) reveal the two fold and three fold symmetries associated with these two loading directions. In all cases, one can detect maximum axial stresses in the center of the specimens and maximum axial strains in the notch roots. As we have shown previously [35,36], stresses redistribute during creep. And an analysis of our data (not explicitly shown here) shows that under the current creep conditions, stresses have already fully redistributed after a few hours. After stress redistribution, we can still observe the effect of anisotropy, but it is significantly less pronounced than the anisotropy associated with pure elastic loading [52,53]. Our results can also be presented in terms of the hydrostatic σ_H and von Mises stress σ_V. We compare these two stress quantities with the axial stress σ_L in Fig. 7, where we show stress profiles starting in the notch root and ending in the center, along the directions indicated by the white arrows shown in Fig. 6. Fig. 7 shows that after 80 h of creep, the [110] specimen shows the highest axial stress and hydrostatic stress in the notch root and the highest von Mises stress, while [111] specimen has the highest σ_L and σ_H in the center of the notch and a low von Mises stress.

Creep behavior: We monitor the creep behavior of the three specimens by measuring the elongation Δ as a function of time and normalizing it by the gauge length L of the double notched specimen (L: 11 mm, Fig. 1)). The ratio Δ/L can be thought of as an average strain ε_{avg}, which does not correspond to an actual physical strain because local strains change along the gauge length of the double notched specimens and have their maxima in the notch root.

In Fig. 8 we show experimental and calculated creep data. Fig. 8a shows the average strains ε_{avg} recorded experimentally for the three loading directions as a function of time. These average strains are derived from the displacement of the whole notch region, where different physical strains accumulate for different cross sections. Fig. 8b shows the corresponding average strain rate data, $\dot{\varepsilon}_{avg}$, as a function of average strain ε_{avg}. Fig. 8c shows the data recorded during the first 100 h (the region highlighted by dashed rectangle in Fig. 8a) at a higher strain resolution, together with the FEM predictions (dashed lines without symbols). As far as strain accumulation is concerned, the creep behavior of the circular notched specimens are affected by damage processes from the beginning on. This is why our primary/secondary crystal plasticity model only predicts the right trends, while the calculated strain data fall short. Fig. 8d shows the corresponding strain rate data up to an average strain value of 0.1 (the region indicated by a dashed vertical line in Fig. 8b). Fig. 8d also shows the predicted average strain rate vs. average strain data obtained by FEM (dashed lines without symbols).

From the experimental data shown in Fig. 8, the rupture times, rupture strains and the minimum average deformation rates are extracted and listed in Table 2.

Fractography, microstructural and crystallographic investigations: Fig. 9 shows SEM images of the rupture surfaces obtained for the three loading directions considered in the present work. The SEM fractographs were taken along the direction as indicated by the black arrow in Fig. 3c. The left column of Fig. 9 shows the overview SEM micrographs of the rupture surfaces. It can be seen that a common feature is that the macroscopic rupture surfaces are always perpendicular to the loading direction, suggesting that failure is normal stress controlled. The regions highlighted by black dashed squares are shown at a higher magnification in

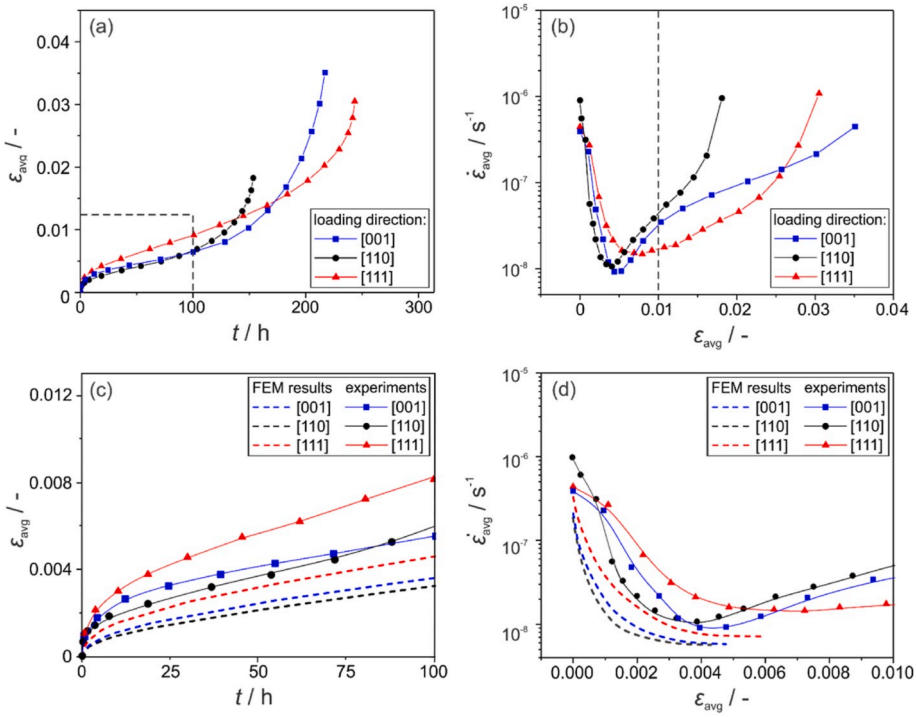

Fig. 8. Creep data of the double notched specimens tested at 950 °C and 400 MPa net section stress. Average strain (ε_{avg}) and average strain rate ($\dot{\varepsilon}_{avg}$) data are shown. (a) and (b): Full creep curves. (c) and (d): Creep data in the primary and secondary creep regimes together with FEM predictions (dashed lines without symbols). (a) and (c) Average creep strain as a function of time. (b) and (d) Average creep strain rates as a function of strain. For details see text.

Table 2
Creep rupture times, minimum deformation rates (derived from average strains) and rupture strains (average strain at rupture). Creep conditions: 950 °C, 400 MPa net section stress. For definition of average strains see text.

Loading direction	Rupture time/h	Minimum rate/s^{-1}	Rupture strain/-
[001]	219	9.10e-9	0.036
[110]	153	1.05e-8	0.019
[111]	243	1.45e-8	0.030

the right column of Fig. 9. The rupture surfaces of the [001] and [110] specimens (Fig. 9a and b) show finer morphologies than that observed on the [111] rupture surface, Fig. 9c. At higher magnifications one can identify local fracture features which point in certain directions as indicated by the dashed white arrows. The terraces on the rupture surfaces even allow to recognize the 4-fold, 2-fold and 3-fold symmetry predicted by crystal plasticity FEM calculations, Fig. 6. In case of the [110] loading direction there are local features which point into [11-2] and [1-12] directions.

In Fig. 10 we show SEM information obtained from central longitudinal cross sections, as indicated by the lower red rectangle in case of the [110] specimen in Fig. 3b. For reasons of comparability, the rupture surfaces are shown at top of the images (not at the bottom as schematically illustrated in Fig. 3b). The SEM micrographs in the first row of Fig. 10 show the ragged rupture surfaces, with the view directions indicated. The upper cross section in Fig. 10c shows that in case of the <111> specimen, the rupture surface deviates significantly from a direction which is perpendicular to the loading direction. Four angles in the range of 40°–50° are indicated. It also appears, that the directions coincide with the alignment of dendritic features in this view direction (for better visibility, dendritic features are marked with white dots). The second row of Fig. 10 presents the EBSD results as color coded IPF (ND) maps (for color coding see standard triangle below the figure).

The results presented in the second row of Fig. 10 clearly show that there are only minor changes in crystal orientations in the longitudinal cross sections of circular notched specimens. The EBSD micrographs presented in the third row of Fig. 10 allow to better appreciate local orientation differences. The images, presented as color coded misorientation to mean orientation maps (color coding presented below the figure as a continuous transition from 0 to 15°) show that there are orientation changes close to the rupture surface, which are particularly pronounced in Fig. 10a ([001] specimen) and 10c ([111] specimen). Without additional information, Fig. 10 does not help to decide whether these local changes have slowly evolved throughout the whole duration of the creep test or whether they represent final rupture events.

Damage in notches shortly before rupture: Our double notch approach allows to obtain exactly this type of information. Fig. 11 shows analytical SEM results from the central longitudinal cross sections of the notches that did not fail. The upper row of Fig. 11 shows SEM micrographs taken using BSE contrast. The second row presents the EBSD results as color coded orientation maps (color coding presented as a standard triangle below the figure). The third row presents EBSD data, evaluated as color coded misorientation to mean orientation maps (color coding presented below the figure as a continuous transition from 0 to 15°).

Characteristic locations are marked with white arrows for reference. The BSE micrographs presented in the upper row of Fig. 11 clearly reveal pore to micro crack transitions in the center of all three specimens (most pronounced in the [001] specimen, left SEM image). The color coded orientation maps in the second row of Fig. 11 suggest that there are only minor changes in overall crystal orientation in the longitudinal cross sections. The data evaluation presented in the last row (misorientation to mean orientation) shows that there are misorientations associated with localized deformation bands and with large local strains accumulated at micro crack tips. In the cross sections of the specimens loaded along the [110] and [111] directions we find twin like features.

Identification of twins: The procedure described in Fig. 5 can be used to identify twins. Fig. 12a and b show the color coded inverse pole figures from the areas marked with white rectangles in Fig. 11b and c (the longitudinal cross sections of the intact notches). Fig. 12c and d show the

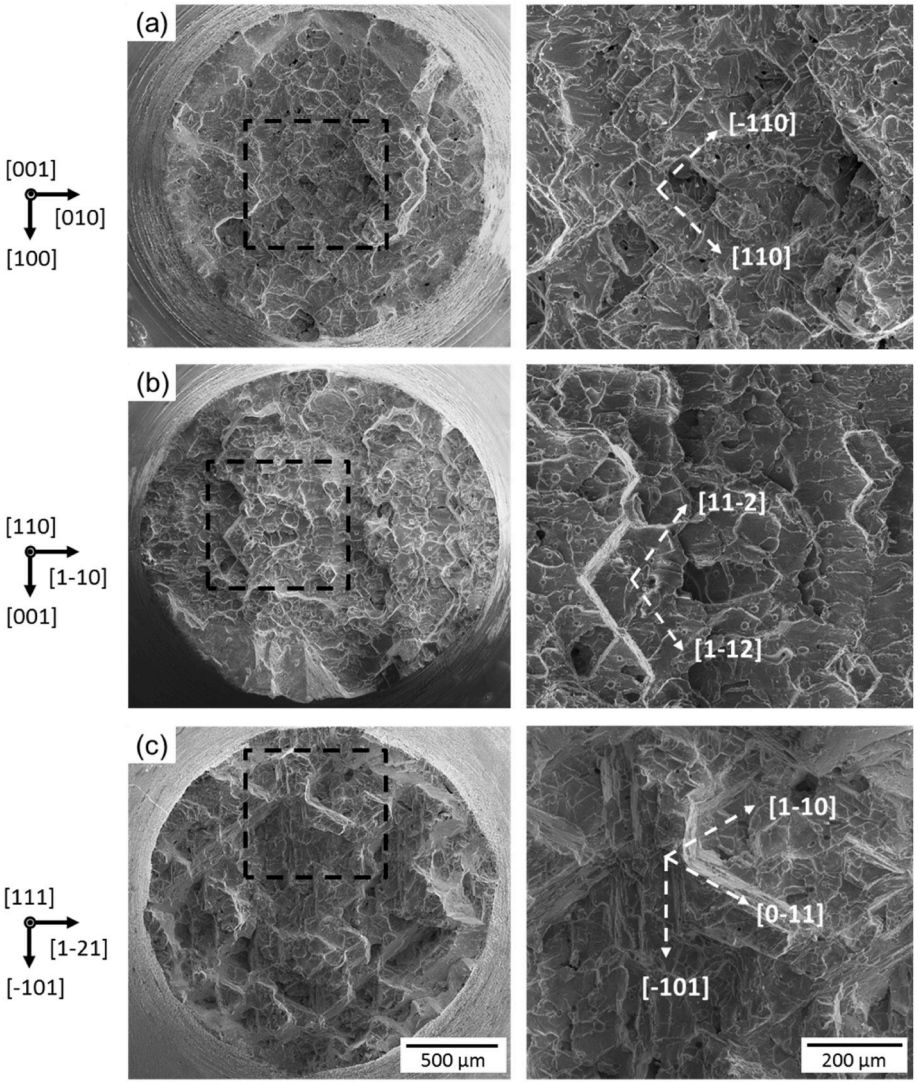

Fig. 9. SEM fractographs of the failed notches after tensile creep loading in [001], [110] and [111] directions. Creep test conditions: 950 °C and 400 MPa net section stress. Left column: Overview images of rupture surfaces. Right column: Rupture surface features at a higher magnification. Crystallographic orientations and crystallographic rupture surface features are indicated. Tensile creep loading directions: (a) [001]. (b) [110]. (c) [111].

areas marked with white rectangles in Fig. 4b and c (the transverse cross sections of the failed notches) at higher magnifications. The crystallographic orientations of the samples are indicated next to the figures.

Fig. 13 shows histograms of rotation angles together with the rotation axes in standard triangles corresponding to the data sets in Fig. 12c and d. The data for [110] and [111] tensile loading are presented in Fig. 13a and b. One can see that for both loading directions a majority of rotation axes are parallel to <111> directions. Moreover, most associated rotation angles represent 60° angles (sharp maxima at 60° in the histograms of Fig. 13a and b). This suggests that they represent coincidence site lattice (CSL) $\sum 3$ twin boundaries [58–60]. No effort was made to quantify twin densities. But one can conclude from the results reported in this section that they yield significant contributions to deformation during the final rupture events.

4. Discussion

Damage accumulation, creep stress and strain analysis: The present work was motivated by research from the McLean group [38–41], who were the first to combine circular double notch creep testing of the single crystal superalloy CMSX-4 with orientation imaging SEM. They observed notch strengthening at 850 °C and net section stresses between 600 to 850 MPa, i.e. their circular notched specimens exposed to net section stresses in this range failed later than uniaxial tensile specimens under equivalent uniaxial stresses. As has been discussed in the literature [28,61–67], this is typically due to the absence of notch root cracking. The absence of notch root cracking and the fact that pores and micro cracks are more frequently observed in the center of the notches for all three loading directions can be clearly seen in Fig. 11. One possible reason is the fast redistribution of the high notch root stress in loading direction during creep [35]. It is shown that under the creep conditions studied in the present work, creep stresses redistribute within the first few hours. After redistribution, both the axial stress and the hydrostatic stress are higher in the center of the notch than in the notch root (Figs. 6 and 7), which is also in good agreement with the fact that micro pores and micro cracks are observed in the center of the specimens, Fig. 11. This represents mechanical support for the notch strengthening results reported in Ref. [38]. The FEM results of the strain and strain rate evolution during creep of double notched specimens shown in Fig. 8c and d predict the right trends, but do not fully reproduce the experimental creep curves. However, not surprisingly, there is a much better fit than that predicted using isotropic FEM calculations which are merely based on a simple Norton law [35]. This is quite typical for creep stress and strain analysis, where it is more difficult to

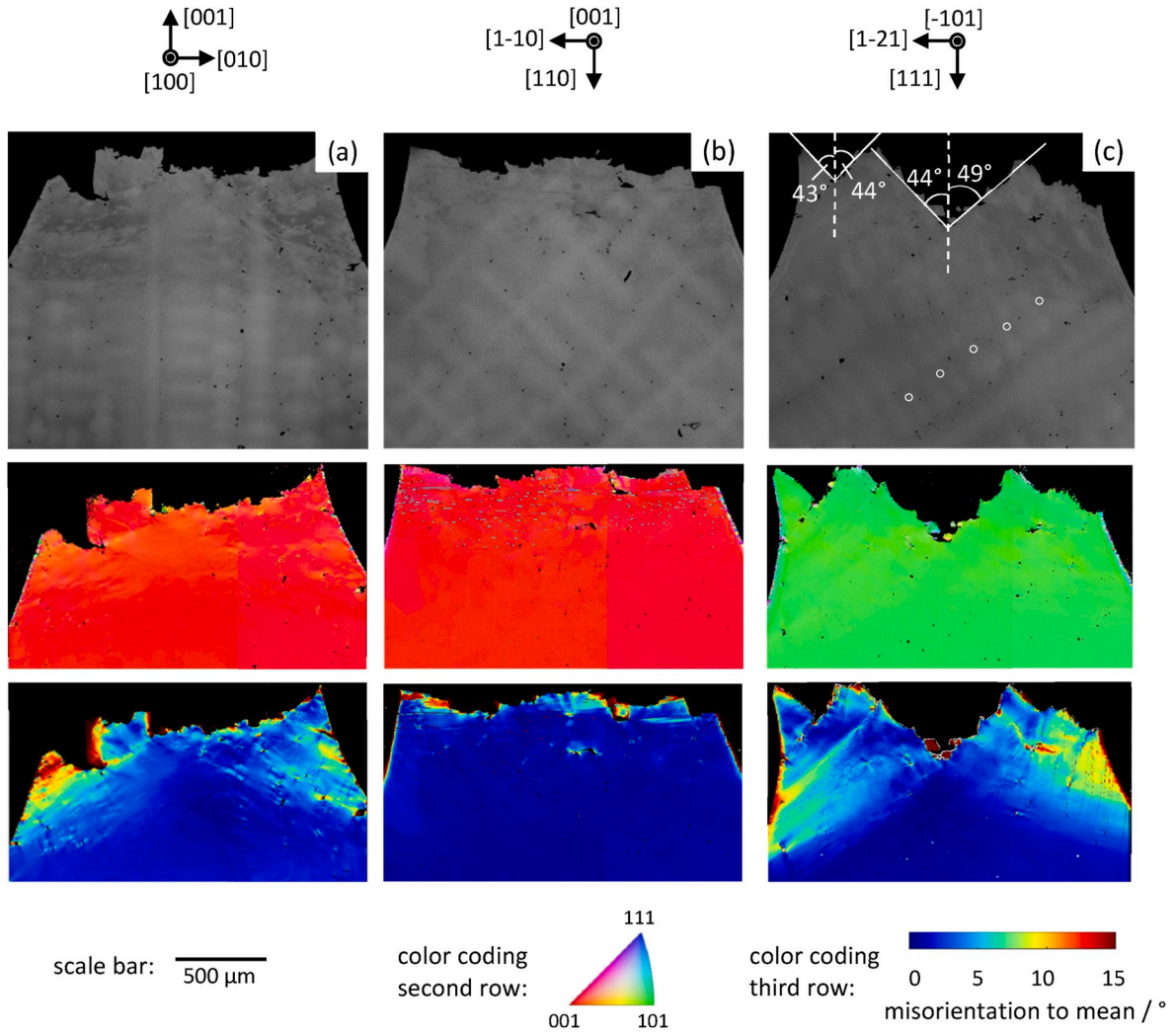

Fig. 10. Microstructural and crystallographic results obtained from the central longitudinal cross sections of the ruptured notch close to the rupture surface (as indicated by the lower red rectangle in Fig. 3b, turned upside down). Upper row: BSE micrographs, for magnification see scale bar below the figure. Middle row: Results from conventional orientation imaging EBSD, for color coding see crystallographic standard triangle below the figure. Bottom row: Evaluation of local misorientations to mean orientation, for color coding see graded transition bar below the figure. Loading directions: (a) [001]. (b) [110]. (c) [111].

predict the right strains (because of the strong stress dependence of the strain rate $\dot{\varepsilon} \tilde{} \sigma^n$) than stresses (which only weekly depend on strain rate $\sigma \tilde{} \dot{\varepsilon}^{1/n}$) [68]. The symmetric distribution of deformation in the transverse notch root cross section predicted by crystal plasticity FEM in Fig. 6 is in good agreement with the symmetric distribution of local lattice rotations observed using orientation imaging SEM, Fig. 4. These effects are very small and can be easily overlooked. In order to make them visible, magnification factors between 30 and 50 were applied. Also, in the color coded inverse pole figures in Fig. 4a and c, some effort was made to identify the four orange regions/three violet regions, where the lattices have rotated towards <101>/<001> directions under [001]/[111] tensile loading conditions. No effort was made to adjust the color coding such that these local orientation differences become visible in Fig. 4b for [110] loading. For this loading condition, a slight geometry change from circular to oval can be directly observed in the inverse pole figure (Fig. 4b) and in the SEM micrograph of the rupture surface, Fig. 9b (image on the left).

On lattice rotation in circular notched SX creep specimens: Our previous results [35,36] have shown, that at uniaxial and net section stresses of 300 MPa, uniaxial specimens accumulated significant amounts of plastic strain (> 20%) while circular notched tensile specimens hardly show any detectable deformation (< 0.04 mm accumulation in a gauge length of 7 mm) [35]. Basoalto et al. [38] reported that for uniaxial loading, large lattice rotations are only observed in creep specimens with tensile axis which deviate from the high symmetric <001> and <111> orientations. They showed that for a specimen loaded in the precise <111> direction, only minor misorientations within 2° were observed. They also claimed (Fig. 9 in Refs. [38]) that very high lattice rotations accompany localized deformation associated with mechanical twinning. In a later paper [39] they reported that the misorientations in the intact notch of a double notched specimen loaded in <111> direction were of the order of ±5° in the notch center, and that higher lattice rotations are only observed in the notch root region. From the results reported in Ref. [38–41] it is not clear whether the formation of twins and the associated lattice rotations govern all stages of multiaxial creep. According to the results obtained in the present work, high lattice rotations are observed in the notch regions, but not confined to the notch root. In the failed notches, large misorientations always occurred in regions very close to the rupture surfaces (Fig. 10), and in the intact notches, large lattice rotations are only observed close to micro pores and micro cracks. This suggests that large lattice rotations accompany the high strain events associated with final rupture. The lattice rotations observed on the transverse cross sections very close to the rupture surfaces in Fig. 4 are also related to final rupture events. One cannot conclude that high symmetry uniaxial testing leads to little lattice rotation while circular

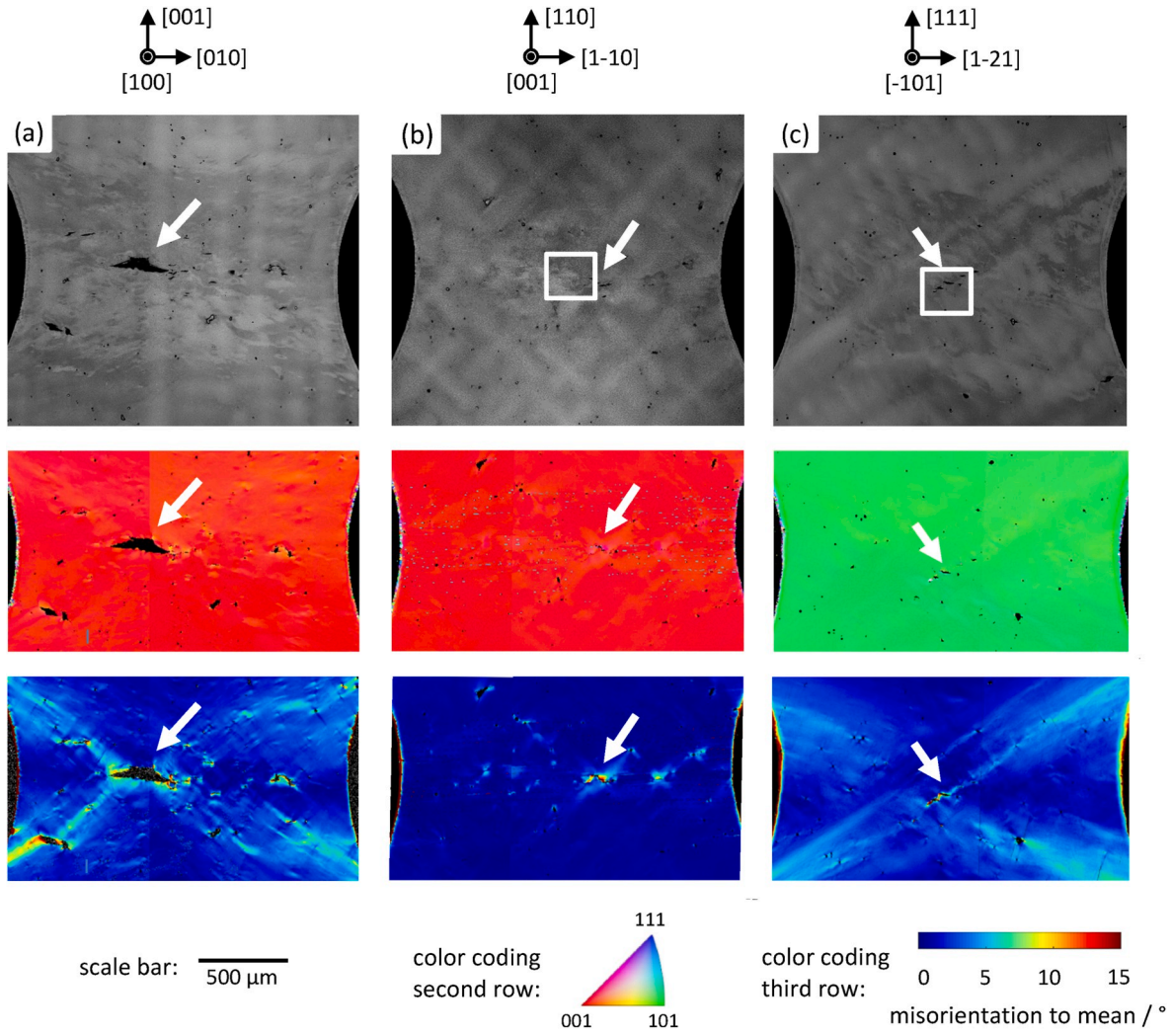

Fig. 11. Microstructural and crystallographic results obtained from central longitudinal cross sections of the second notch which did not rupture. Upper row: BSE micrographs, for magnification see scale bar below the figure. Middle row: Results from conventional orientation imaging EBSD, for color coding see crystallographic standard triangle below the figure. Bottom row: Evaluation of local misorientations to mean orientation, for color coding see graded transition bar below the figure. Loading directions: (a) [001]. (b) [110]. (c) [111].

notched multiaxial testing does, as was concluded in Ref. [38].

Observation *of deformation twins*: It has been reported in the literature that twinning is a deformation mode which can occur during low temperature and high stress creep of single crystal Ni-base superalloys under uniaxial and multiaxial stress states [21,40,42,69–73]. Twins are associated with dislocation ribbons, where four individual dislocations combine to facilitate γ'-phase cutting. Twins are known to form on {111} planes with displacement vectors of type <112>. The slip directions and slip planes together with the Schmid factors which act in these micrographic crystallographic shear systems under [110] and [111] uniaxial loading are listed in Table 3.

The fact that twins are observed after creep of SXs at intermediate temperature was already reported by the McLean group [40,42]. In the present work we have shown that for [110] loading twins formed in a relatively larger region in the notch, while for [111] loading twinning is confined to areas very close to micro cracks and rupture surfaces, Figs. 10–12 (difficult to see due to small image sizes but possible to appreciate). The current study also went one step further and identified the different twin variants, Figs. 5, 12 and 13. The fact that two respectively three twin variants are identified during [110] and [111] tensile creep testing is in line with the fact that two respectively three microscopic crystallographic twin systems (indicated in bold in Table 3) are most strongly promoted during [110] and [111] loading. We have also shown that twinning is associated with misorientations of 60° around <111> rotation axes, Fig. 13. However, twinning does not necessarily result in large-scale lattice rotations of the matrix surrounding the twins, as can be clearly seen in the middle row of Fig. 11. Further work is required to study the spatial distribution of damage in the notch root cross section and the effect of the multiaxial stress state on dislocation plasticity.

5. Summary and conclusions

In the present work, we use a miniature double notched specimen to investigate the anisotropic creep rupture behavior of the Ni-base single crystal superalloy ERBO/1 at 950 °C and a net section stress of 400 MPa. We conduct tensile creep tests in three loading directions [001], [110] and [111]. One advantage of using miniature tensile creep specimens is that only small amount of material is needed and therefore specimens can be taken out from laboratory scale single crystal slabs. A key advantage of testing double notched specimens is that after one notch fails, the other notch is still intact and represents a material state shortly before rupture. This allows to characterize the microstructural damage shortly before the onset of final rupture. From the results obtained in the present work the following conclusions can be drawn:

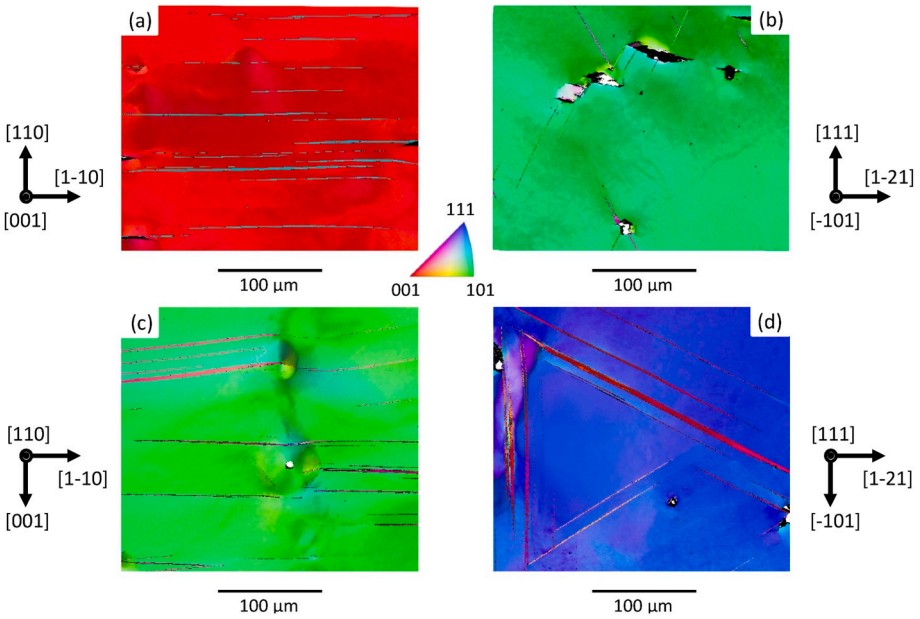

Fig. 12. Inverse pole figure orientation maps. (a) Longitudinal cross section of the intact notch after [110] rupture. (b) Longitudinal cross section of the intact notch after [111] rupture. (c) Transverse cross section of the failed notch after [110] rupture. (d) Transverse cross section of the failed notch after [111] rupture.

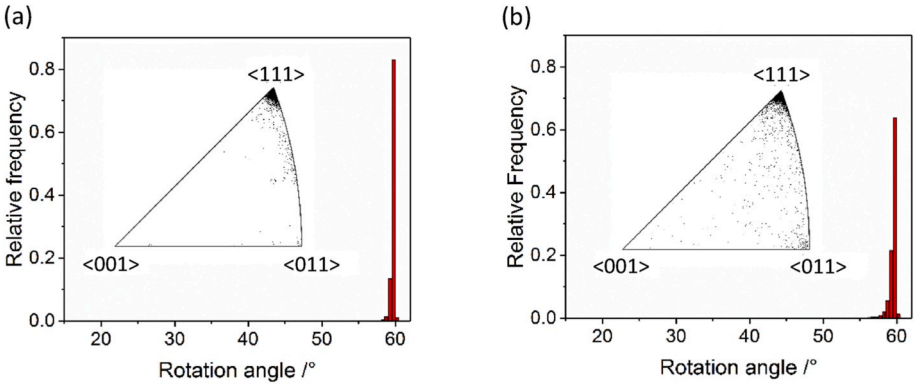

Fig. 13. Histograms showing distributions of rotation angles together with spread of rotation axes of the twins in inverse pole figures. (a) [110] tensile loading. (b) [111] tensile loading.

Table 3
Twelve microscopic crystallographic twin systems together with the corresponding Schmid factors (SFs) during [110] and [111] tensile loading. The slip systems with the highest Schmid factors are indicated in bold.

Slip direction	Slip plane	SFs in [110]experiments	SFs in [111]experiments
$[\bar{2}11]$	(111)	0.236	0
$[1\bar{2}1]$	(111)	0.236	0
$[11\bar{2}]$	**(111)**	**0.471**	0
$[2\bar{1}1]$	$(\bar{1}\bar{1}1)$	0.236	0.157
$[2\bar{1}1]$	$(\bar{1}\bar{1}1)$	0.236	0.157
$[\bar{1}\bar{1}2]$	**$(\bar{1}\bar{1}1)$**	**0.471**	**0.314**
$[\bar{2}\bar{1}1]$	**$(1\bar{1}\bar{1})$**	0	**0.314**
$[12\bar{1}]$	$(1\bar{1}\bar{1})$	0	0.157
$[1\bar{1}2]$	$(1\bar{1}\bar{1})$	0	0.157
$[21\bar{1}]$	$(\bar{1}1\bar{1})$	0	0.157
$[\bar{1}2\bar{1}]$	**$(\bar{1}1\bar{1})$**	0	**0.314**
$[\bar{1}12]$	$(\bar{1}1\bar{1})$	0	0.157

(1) The anisotropic finite element stress and strain analysis (FEM) performed in the present work yields three results: First, there is a reasonable agreement between FEM predictions and measured displacements during creep of double notched specimens. Second, after stresses have redistributed under creep conditions, the maximum principal stress and hydrostatic stress are highest in the center of the specimens and lowest in the notch root, while the von Mises stress is almost homogeneous all over the notch root cross section. And finally, the deformation symmetry ([001] loading: 4-fold, [110] loading: 2-fold and [111] loading: 3-fold) predicted by crystal plasticity based FEM calculations can be experimentally confirmed.

(2) In agreement with the FEM predictions, no notch root cracking was observed in the notch root and pores and micro cracks formed in the center of the intact notches. This was observed for all three crystallographic loading directions, which indicates that the maximum principal stress and hydrostatic stress are dominant parameters of the load spectrum.

(3) Mechanical twinning was observed and the twins were identified as <112>{111} type of planar faults, in agreement with what has been reported for low temperature and high stress creep in the literature. A micromechanical analysis showed that the expected

two/three twin variants were indeed detected after <110>/<111> tensile creep testing. In case of the <110> loading, twinning was not confined to the notch root regions or areas close to micro cracks, but was observed in wider regions of the notches.

(4) Local maximum misorientations in circular notched miniature tensile creep specimens after rupture can be as high as 15°. This was, however, only observed in regions close to rupture surfaces (ruptured notches of double notched specimens) and micro cracks and pores (central regions of intact notches of double notched specimens). One important result of the present work is that these high lattice rotations do not evolve gradually throughout multiaxial creep testing. They are associated with the high strain events (necking) which occur during final rupture.

(5) What remains to be investigated is how the microstructural damage (pores and micro cracks) is spatially distributed and how the multiaxial stress state in combination with the crystallographic loading direction affects dislocation plasticity. Further work is under way to clarify these points.

Declaration of competing interest

The authors declare that they have no known competing financial interests or personal relationships that could have appeared to influence the work reported in this paper.

CRediT authorship contribution statement

L. Cao: Conceptualization, Methodology, Writing - original draft, Funding acquisition. **P. Thome:** Software, Formal analysis, Visualization, Writing - review & editing. **L. Agudo Jácome:** Visualization, Funding acquisition. **C. Somsen:** Supervision, Writing - review & editing. **G. Cailletaud:** Software, Writing - review & editing, Funding acquisition. **G. Eggeler:** Conceptualization, Writing - review & editing, Funding acquisition.

Acknowledgements

All authors acknowledge funding through projects A1 and A2 of the collaborative research center SFB/TR 103 on superalloy single crystals. LC acknowledges funding from the China Scholarship Council (File No. 201406830001) and support by the International Max Planck Research School SurMat. GC acknowledges funding through the Safran-Mines Paristech “Cristal” research chair on high-temperature materials. LAJ acknowledges funding by the German Research Association (DFG) through project AG 191/1-1.

References

[1] G.W. Meetham, The Development of Gas Turbine Materials, Applied Science Publishers, London, 1981.
[2] M. McLean, Directionally Solidified Materials for High Temperature Service, Metals Society London, London, 1983.
[3] M. Durand-Charre, The Microstructure of Superalloys, CRC Press, Boca Raton, 1997.
[4] M.J. Donachie, S.J. Donachie, Superalloys: A Technical Guide, ASM International, Materials Park, Ohio, 2002.
[5] R.C. Reed, The Superalloys: Fundamentals and Applications, Cambridge university press, Cambridge, 2006.
[6] T.M. Pollock, S. Tin, Nickel-based superalloys for advanced turbine engines: chemistry, microstructure and properties, J. Propul. Power 22 (2006) 361–374.
[7] B. Geddes, H. Leon, X. Huang, Superalloys: Alloying and Performance, ASM International, Materials Park, Ohio, 2010.
[8] R. Bürgel, H.J. Maier, T. Niendorf, Handbuch Hochtemperatur-Werkstofftechnik, Vieweg + Teubner Verlag, Wiesbaden, 2011.
[9] M.E. Kassner, Fundamentals of Creep in Metals and Alloys, Elsevier, Amsterdam, 2009.
[10] B. Ilschner, Hochtemperaturplastizität, Springer Verlag, Berlin, 1973.
[11] R.W. Evans, B. Wilshire, Creep of Metals and Alloys, Institute of Materials, London, 1985.
[12] J.-P. Poirier, Creep of Crystals: High-Temperature Deformation Processes in Metals, Ceramics and Minerals, Cambridge University Press, Cambridge, 1985.
[13] J. Čadek, Creep in Metallic Materials, Elsevier, Amsterdam, 1988.
[14] F.R.N. Nabarro, H.L. deVilliers, The Physics of Creep, Taylor and Francis, London, 1995.
[15] C. Mayr, G. Eggeler, G.A. Webster, G. Peter, Double shear creep testing of superalloy single crystals at temperatures above 1000 °C, Mater. Sci. Eng. A. 199 (1995) 121–130.
[16] M. Kamaraj, C. Mayr, M. Kolbe, G. Eggeler, On the influence of stress state on rafting in the single crystal superalloy CMSX-6 under conditions of high temperature and low stress creep, Scripta Mater. 38 (1998) 589–594.
[17] K. Serin, G. Göbenli, G. Eggeler, On the influence of stress state, stress level and temperature on γ-channel widening in the single crystal superalloy CMSX-4, Mater. Sci. Eng. A. 387–389 (2004) 133–137.
[18] V. Caccuri, J. Cormier, R. Desmorat, γ′-rafting mechanisms under complex mechanical stress state in Ni-based single crystalline superalloys, Mater. Des. 131 (2017) 487–497.
[19] B. Fedelich, A. Epishin, T. Link, H. Klingelhöffer, G. Künecke, P.D. Portella, Experimental characterization and mechanical modeling of creep induced rafting in superalloys, Comput. Mater. Sci. 64 (2012) 2–6.
[20] B. Fedelich, A. Epishin, T. Link, H. Klingelhöffer, G. Künecke, P.D. Portella, Rafting during high temperature deformation in a single crystal superalloy, in: S. Huron, et al. (Eds.), Superalloys 2012, Proc. Of the 12th International Symposium on Superalloys, TMS, Warrendale, 2012, pp. 491–500.
[21] J.-B. le Graverend, F. Pettinari-Sturmel, J. Cormier, M. Hantcherli, P. Villechaise, J. Douin, Mechanical twinning in Ni-based single crystal superalloys during multiaxial creep at 1050 °C, Mater. Sci. Eng. A. 722 (2018) 76–87.
[22] M. Kamaraj, Rafting in single crystal nickel-base superalloys – an overview, Sadhana - Acad. Proc. Eng. Sci. 28 (2003) 115–128.
[23] H. Neuber, Kerbspannungslehre – Theorie der Spannungskonzentration, Genaue Berechnuntg der Festigkeit, second ed., Springer Verlag, Berlin, 1958.
[24] R.E. Peterson, Stress Concentration Factors, Wiley, New York, 1974.
[25] G.E. Dieter, Mechanical Metallurgy, McGraw Hill, London, 1988.
[26] G. Owolabi, O. Okeyoyin, O. Bamiduro, A. Olasumboye, H. Whitworth, The effects of notch size and material microstructure on the notch sensitivity factor for notched components, Eng. Fract. Mech. 145 (2015) 181–196.
[27] P. Lukáš, P. Preclík, J. Čadek, Notch effects on creep behaviour of CMSX-4 superalloy single crystals, Mater. Sci. Eng. A. 298 (2001) 84–89.
[28] G. Eggeler, C. Wiesner, A numerical study of parameters controlling stress redistribution in circular notched specimens during creep, J. Strain Anal. Eng. Des. 28 (1993) 13–22.
[29] D. Wu, E.M. Christian, E.G. Ellison, Influence of constraint on creep stress distribution in notched bars, J. Strain Anal. Eng. Des. 19 (1984) 209–220.
[30] D.R. Hayhurst, F.A. Leckie, J.T. Henderson, Design of notched bars for creep rupture testing under triaxial stresses, Int. J. Mech. Sci. 19 (1977) 147–159.
[31] D.R. Hayhurst, J.T. Henderson, Creep stress redistribution in notched bars, Int. J. Mech. Sci. 19 (1977) 133–146.
[32] D.R. Hayhurst, G.A. Webster, An overview on studies of stress state effects during creep of circumferentially notched bars, in: D.J. Gooch, I.M. How (Eds.), Tech. Multiaxial Creep Test., Springer Verlag, Netherlands, Dordrecht, 1986.
[33] W.D. Nix, J.C. Earthman, G. Eggeler, B. Ilschner, The principal facet stress as a parameter for predicting creep rupture under multiaxial stresses, Acta Metall. 37 (1989) 1067–1077.
[34] A.M. Agogino, Notch effects, stress state, and ductility, J. Eng. Mater. Technol. 100 (1978) 348–355.
[35] L. Cao, D. Bürger, P. Wollgramm, K. Neuking, G. Eggeler, Testing of Ni-base superalloy single crystals with circular notched miniature tensile creep (CNMTC) specimens, Mater. Sci. Eng. A. 712 (2018) 223–231.
[36] L. Cao, P. Wollgramm, D. Bürger, A. Kostka, G. Cailletaud, G. Eggeler, How evolving multiaxial stress states affect the kinetics of rafting during creep of single crystal Ni-base superalloys, Acta Mater. 158 (2018) 381–392.
[37] P. Boubidi, Experimental characterization and numerical modelling of low cycle fatigue in a nickel base single crystal superalloy under multiaxial loading, Ecole des Mines, Doctoral dissertation, 2000.
[38] H.C. Basoalto, R.N. Ghosh, M.G. Ardakani, B.A. Shollock, M. McLean, Multiaxial creep deformation of single crystal superalloys: modelling and validation, Superalloys 2000 (2000) 515–524.
[39] H.C. Basoalto, M. Ardakani, R.N. Ghosh, M. McLean, Multiaxial lifetime predictions of single-crystal superalloys: use of reference stresses, Mater. Manuf. Process. 17 (2002) 519–528.
[40] M. Ardakani, H. Basoalto, B.A. Shollock, M. McLean, Characterisation and modelling of crystal rotations during multiaxial creep in single crystal superalloys, Mater. Sci. Forum 426 (2003) 797–802.
[41] M. Ardakani, H. Basoalto, B.A. Shollock, M. McLean, Lattice rotations during creep deformation of a single crystal superalloy in triaxial stresses, Adv. Mech. Behav. Plast. 1 (2000) 335–340.
[42] M.G. Ardakani, M. McLean, B.A. Shollock, Twin formation during creep in single crystals of nickel-based superalloys, Acta Mater. 47 (1999) 2593–2602.
[43] G.R. Leverant, B.H. Kear, The mechanism of creep in gamma prime precipitation-hardened nickel-base alloys at intermediate temperatures, Metall. Mater. Trans. B 1 (1970) 491–498.
[44] G.R. Leverant, B.H. Kear, J.M. Oblak, Creep of precipitation-hardened nickel-base alloy single crystals at high temperatures, Metall. Trans. 4 (1973) 355–362.
[45] M. McLean, R.N. Ghosh, R.V. Curtis, U. Basu-Conlin, M.R. Winstone, Anisotropy of high temperature deformation of single crystal superalloys-constitutive laws modelling and validation, Superalloys 992 (1992) 609–618, 1992.
[46] G. Eggeler, Microstructural parameters for creep damage accumulation, Acta Metall. Mater. 39 (1991) 221–231.

[47] M. Cans, G. Eggeler, On the influence of grain morphology on creep rupture times of cavitating materials, Scripta Metall. Mater. 30 (1994) 107–112.
[48] A.B. Parsa, P. Wollgramm, H. Buck, C. Somsen, A. Kostka, I. Povstugar, P.P. Choi, D. Raabe, A. Dlouhy, J. Müller, E. Spiecker, K. Demtroder, J. Schreuer, K. Neuking, G. Eggeler, Advanced scale bridging microstructure analysis of single crystal Ni-base superalloys, Adv. Eng. Mater. 17 (2015) 216–230.
[49] G. Mälzer, R.W. Hayes, T. Mack, G. Eggeler, Miniature specimen assessment of creep of the single-crystal superalloy LEK 94 in the 1000°C temperature range, Metall. Mater. Trans. 38 (2007) 314–327.
[50] G.A. Webster, S.R. Holdsworth, M.S. Loveday, K.M. Nikbin, I.J. Perrin, H. Purper, R.P. Skelton, M.W. Spindler, A Code of Practice for conducting notched bar creep tests, Fatig. Fract. Eng. Mater. Struct. 27 (2004) 319–342.
[51] P. Wollgramm, D. Bürger, A.B. Parsa, K. Neuking, G. Eggeler, The effect of stress, temperature and loading direction on the creep behaviour of Ni-base single crystal superalloy miniature tensile specimens, Mater. A. T. High. Temp. 33 (2016) 346–360.
[52] L. Méric, P. Poubanne, G. Cailletaud, Single crystal modelling for structural calculations: Part 1-modal presentation, J. Eng. Mater. Technol. 113 (1991) 162–170.
[53] L. Méric, G. Cailletaud, Single crystal modelling for structural calculations: Part 2-finite element implementation, J. Eng. Mater. Technol. 113 (1991) 171–182.
[54] Z-set user commands, Version 9.0, Material & Structure Analysis Suite, 2018. www.zset-software.com.
[55] H. Benker, Mathematik mit MATLAB, Springer Verlag, Berlin Heidelberg, 2000.
[56] R. Hielscher, H. Schaeben, A novel pole figure inversion method: specification of the MTEX algorithm, J. Appl. Crystallogr. 41 (2008) 1024–1037.
[57] F. Bachmann, R. Hielscher, H. Schaeben, Texture analysis with MTEX - free and open source software toolbox, Solid State Phenom. 160 (2010) 63–68.
[58] V. Randle, The coincidence site lattice and the "sigma enigma", Mater. Char. 47 (2001) 411–416.
[59] V. Randle, "Five-parameter" analysis of grain boundary networks by electron backscatter diffraction, J. Microsc. 222 (2006) 69–75.
[60] R.W. Balluffi, A. Brokman, A.H. King, CSL/DSC Lattice model for general crystal boundaries and their line defects, Acta Metall. 30 (1982) 1453–1470.
[61] A. Manonukul, F.P.E. Dunne, D. Knowles, S. Williams, Multiaxial creep and cyclic plasticity in nickel-base superalloy C263, Int. J. Plast. 21 (2005) 1–20.
[62] D.R. Hayhurst, P.R. Dimmer, C.J. Morrison, Development of Continuum Damage in the Creep Rupture of Notched Bars, vol. 311, 1984, pp. 103–129.
[63] A.M. Othman, J. Lin, D.R. Hayhurst, B.F. Dyson, Comparison of creep rupture lifetimes of single and double notched tensile bars, Acta Metall. Mater. 41 (1993) 1215–1222.
[64] A.H. Sherry, R. Pilkington, The creep behaviour of a Nickel-based single-crystal superalloy, Mater. Sci. Eng. 82 (1986) 27–36.
[65] A.M. Hashem, D. Goldschmidt, E. El-Magd, Cavitation damage of the single-crystal nickel-base superalloy SRR99 during creep at 850°C, Mater. Werkst. 25 (1994) 133–138.
[66] B.F. Dyson, M.S. Loveday, Creep fracture in Nimonic 80A under triaxial tensile stressing, Creep Struct. (1981) 406–421.
[67] D.R. Hayhurst, J. Lin, R.J. Hayhurst, Failure in notched tension bars due to high-temperature creep: interaction between nucleation controlled cavity growth and continuum cavity growth, Int. J. Solid Struct. 45 (2008) 2233–2250.
[68] J.T. Boyle, J. Spence, Stress Analysis for Creep, Butterworth Heinemann, London, 1983.
[69] B. Kear, J. Oblak, Deformation modes γ′-precipitation hardened Ni-base superalloy, J. Phys. Colloq. 35 (1974) 35–45.
[70] D. Barba, E. Alabort, S. Pedrazzini, D.M. Collins, A.J. Wilkinson, P.A.J. Bagot, M. P. Moody, C. Atkinson, A. Jérusalem, R.C. Reed, On the microtwinning mechanism in a single crystal superalloy, Acta Mater. 135 (2017) 314–329.
[71] D. Barba, S. Pedrazzini, A. Vilalta-Clemente, A.J. Wilkinson, M.P. Moody, P.A. J. Bagot, A. Jérusalem, R.C. Reed, On the composition of microtwins in a single crystal nickel-based superalloy, Scripta Mater. 127 (2017) 37–40.
[72] X. Wu, A. Dlouhy, Y.M. Eggeler, E. Spiecker, A. Kostka, C. Somsen, G. Eggeler, On the nucleation of planar faults during low temperature and high stress creep of single crystal Ni-base superalloys, Acta Mater. 144 (2018) 642–655.
[73] C.M.F. Rae, R.C. Reed, Primary creep in single crystal superalloys: origins, mechanisms and effects, Acta Mater. 55 (2007) 1067–1081.